Ocean Sound Speed Profile Measurement Using a Pulse-Echo Technique

Mohammad Reza Mousavi, and Len Zedel

Abstract

This paper presents an acoustic method for remotely measuring the ocean sound speed profile using a single directional transmitter and at least two receivers. By employing cross-correlation techniques to estimate the time of flight of echo-received signals, the proposed approach calculates both the average sound speeds and the depths of ocean reflectors, resulting in the estimation of the sound speed profile. To validate the method, simulations are conducted using a ray acoustic propagation model that includes both time-invariant conditions and time-varying statistical effects. Key factors such as pulse length, number of pulse repetitions, transducer beam width, transducer arrangement, signal-to-noise ratio, and reflector density are analyzed. The accuracy of the estimated sound speed profiles is assessed by comparing them with the input profiles used in the simulation model. Using the proposed approach, a non-uniform sound speed profile is measured with a root mean square error of 2.1 m/s up to 125 m, highlighting its practicality for ocean sound speed monitoring. The method is also experimentally evaluated in a controlled tank environment with a nearly constant sound speed. The estimated sound speed profile has a standard deviation of 3.23 m/s relative to the expected value in tank test.

Index Terms

Ocean Sound speed profile, remote measurement, pulse-echo technique.

I. Introduction

The ocean Sound Speed Profile (SSP) is an important parameter in underwater acoustic directly influencing the behavior of acoustic wave propagation. In applications such as multibeam sonar or Synthetic Aperture Sonar (SAS), as well as acoustic localization and tracking, accurate SSP data is essential for extracting accurate measurements. High-resolution underwater imaging in marine biology, geology, and oil and gas exploration also rely heavily on accurate SSP information.

Current methods, such as the use of Conductivity, Temperature, Depth (CTD) data or direct Sound Velocity Profilers (SVP) systems, require vessels to stop for data collection, which is costly, time-consuming, and can disrupt data collection. Alternatives that enable data collection from a moving vessel, such as eXpendable BathyThermographs (XBT), eXpendable Conductivity, Temperature, Depth (XCTD) systems, or Moving Vessel Profilers (MVPs), can provide high-quality SSP but often come with trade-offs. These trade-offs include the need for deck space, maintenance requirements, and potentially significant costs, particularly for large-scale or deep-water operations.

This paper introduces an acoustic approach for remotely measuring the ocean's SSP. There have been previous studies that have explored the possibility of underwater SSP estimation through acoustic methods [1]–[3]. Our previous method [1] for remote SSP measurement required the use of a highly directional narrow beam transducer, which is not always possible, particularly when operating at low frequencies. The fundamental concept in [2] involves a known source, reflector, and receiver geometry used to establish a travel distance. It then utilizes precise time measurements to estimate sound speed. However, [2] assumes that signals transmitted at different angles and slightly different frequencies undergo similar channel responses, which may explain limited success in field trials. Brumley [3] identifies techniques similar to geophysical seismic exploration, focusing on measuring the curvature of reflected waveforms. However, this approach typically necessitates a lengthy receiver array. Some researchers have applied actual geophysical methods to explore sound speed and, by extension, ocean temperature structures [4], [5]. These techniques pose limitations for general oceanographic applications due to the extensive receiver arrays they require, often spanning several kilometers, and their limited depth resolution.

Knowledge of sound speed profiles is essential not only in oceanographic and seismic studies but also in the domain of medical science (see, [6]–[14]). Interestingly, there appears to be a distinct separation between these two fields regarding interaction and knowledge exchange in estimating SSP. Research in the medical science domain focuses on enhancing the quality of ultrasound imaging by calculating the SSP within body tissues. In addition, the speed of sound within the human body varies with tissue conditions, so knowledge of sound speed has the potential to be a tool to measure tissue properties.

Medical SSP investigations are typically classified into two primary categories: transmission methods and pulse-echo methods. Historically, medical tomography has mainly focused on transmission methods, characterized by the need for accessibility from both sides of the region of interest. This is directly analogous to what is done in ocean acoustic tomography [15]. Our present study centers on exploring pulse-echo methods for SSP estimation. This choice is deliberate, as we aim to estimate SSP with a source-receiver system located at the sea surface.

Robinson *et al.* [7] extensively reviewed early work on pulse-echo sound speed estimation methods in medical science and identified three techniques for estimating sound speed. The first technique exploits apparent location shifts of the target from two angles, using different directions of signal transmission and reception. An incorrect sound speed causes blurring and/or shifting in the location of targets in different views. Quantifying the target shift [16], [17] or varying the sound speed value by the operator to obtain the clearest ultrasound image [18] allows for sound speed estimation. The second technique estimates the sound speed by measuring pulse transmission times and path lengths. The path length can be determined using the known geometry of intersecting coplanar beams between the transmitter and receivers and travel time estimation through the echo signals [19]. The third technique uses the transaxial deformation of the image of a flat reflector [20]; that is the idea that if a region has a raised/lowered sound speed, it shifts toward/away from the transducer in the ultrasound image.

More recently, Anderson and Trahey [8] presented a method similar to that used in seismology exploration using a long transducer array. They estimated the location of the reflector and the average sound speed using the curvature of the reflected wave. However, they assumed a known sound speed during the beamforming process, a simplification that may not always hold true. This assumption introduces bias into the measurement of the average sound speed, as it depends on the sound speed utilized in beamforming. Further investigations by Jakovljevic *et al.* [12] used the average sound speed estimation concept introduced in [8] and then proposed a model to relate the local sound speed to the average sound speed. Ali *et al.* [13] and Ali and Dahl [14] present another method by employing a coherence-based approach in conjunction with dynamic focusing delays at both the transmitter and receiver. This concept of dynamic delays has also been used by Yoon *et al.* [11]. In contrast to the majority of methods in the medical community that employ an array of transducers to measure sound speed, [9] uses a single transducer and two receivers in distinct locations. Sound speed is estimated by minimizing the Root Mean Square (RMS) error between a time-delay profile determined by received signals and a theoretical time-delay profile. This approach assumes a zero-beam width approximation, impractical in many ocean applications.

Most of the methods proposed in medical and geophysical science rely on large arrays (relative to the sampling depth interval) employing many transducer elements; this article presents a technique that does not require a large array. The main idea of this paper is to estimate the sound speed using the theoretical and experimental time-delay profile. Our approach utilizes one directional transmitter and a minimum of two receivers to estimate the average sound speed between the transducer and reflector depth. The reflector depth is itself treated as an unknown random variable. Average sound speeds and reflector depths are estimated by measuring the arrival times and delays of echoes at receivers and then minimizing the RMS difference between this measured time-delay profile and the theoretically predicted values.

We evaluate the performance of our method using simulated received signals generated by an acoustic propagation model. The model is based on ray acoustic propagation, excluding lateral sound speed variations and assuming that rays propagate straight paths without bending. To test the validity of our method, the estimated SSP is compared to the one used in the simulation of the synthetic received signal. Simulation analysis explores parameters, including the effect of pulse repetitions, pulse length, beam width of transducers, reflector density, Signal-to-Noise Ratio (SNR), and transducer geometry. To extract SSP from the average SSP, we employ the technique introduced by [13].

The method was experimentally validated in the 200 m towing tank of the National Research Council of Canada (NRC) in St. John's, Canada, using a Furuno DFF3-UHD unit as a 100 kHz pulse generator and a custom receiver system equipped with two side-scan transducers. By moving suspended reflectors along the length of the tank using the overhead carrier of the facility, the experiment simulated vertical profiling in ocean environments and allowed evaluation of the performance of the method under controlled conditions.

The remainder of the paper is structured as follows. Section II outlines our average SSP estimation technique. Section III details our model for simulating the reflected signal at the receivers and reviews the relationship between local and average sound speed. Section IV presents the simulation results and compares the SSPs estimated by our approach with "ground truth" from the signal model. Section V describes the experimental validation of the method in a controlled tank environment. We conclude in section VI with closing remarks on our research. Finally, in Appendix, the approximation of non-bending ray propagation is discussed.

II. The Sound Speed Estimation

To estimate SSP, one transmitter and two receivers are used. The schematic representation of our proposed method is depicted in Fig. 1. Within this illustration, T denotes the acoustic transmitter, while R_1 and R_2 represent two receivers positioned at distances d_1 and d_2, respectively, from transmitter. All transducers are located at depth h. The transmitted acoustic beam ensonifies the ocean volume, encountering reflectors scattered randomly within. These reflectors could be marine organisms such as fish or plankton. The reflectors are randomly distributed in three dimensions within the ensonified volume, and this three-dimensional spatial distribution is taken into account in both the theoretical derivations and the signal simulation. Subsequently, the reflected signals are recorded by the receivers R_1 and R_2.

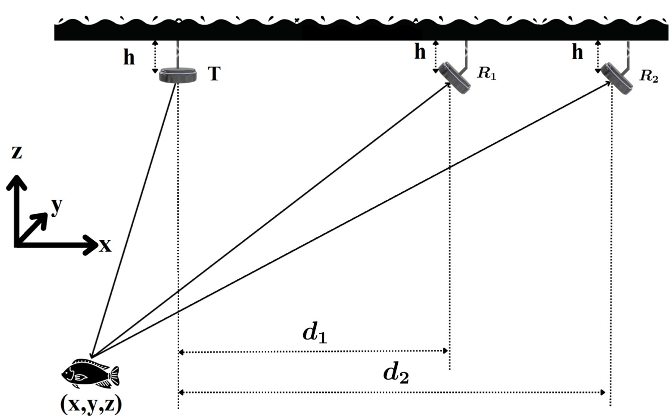

Fig. 1: Method geometry including the transducers and reflector at (x, y, z).

The core concept of our approach is deriving the theoretical time-delay profile between two received signals from receivers R_1 and R_2 and subsequently estimating the sound speed by minimizing the RMS difference between this theoretical time-delay profile and the experimentally observed time-delay profile.

In our approach, we assume that ray propagation follows straight paths without bending. This assumption holds true when variations in sound speed are negligible compared to the average sound speed along each path or when the angles between the rays and the vertical line to the transducers are small (See Appendix). To find the theoretical time-delay profile, consider a transmitter at the origin and a reflector at (x, y, z). According to Fig. 1, the distance traveled by the ray connecting the transmitter to the reflector, and subsequently received by receivers R_1 and R_2, can be expressed as follows:

$$r_1 = \sqrt{x^2 + y^2 + z^2} + \sqrt{(x - d_1)^2 + y^2 + z^2}, \tag{1}$$

and

$$r_2 = \sqrt{x^2 + y^2 + z^2} + \sqrt{(x - d_2)^2 + y^2 + z^2}. \tag{2}$$

Assume that the relationship between $\Delta r = r_2 - r_1$ and r_1 can be approximated by a polynomial of degree n, so:

$$\Delta r = a_n {r_1}^n + a_{n-1} {r_1}^{n-1} + ... + a_1 r_1 + a_0, \tag{3}$$

also, assume the relation between r_1 and z can be approximated by a polynomial of degree m, hence:

$$r_1 = b_m z^m + b_{m-1} z^{m-1} + ... + b_1 z + b_0. \tag{4}$$

Polynomial fits are invoked here because the combination of (1) and (2) with the complex sampling domain of bisecting acoustic beams would otherwise give rise to a non-standard mathematical form.

To determine the coefficients a_i and b_i in equations (3) and (4), a least-squares polynomial fitting approach is used. Using N simulated, randomly distributed reflectors and evaluating the corresponding $(r_1, \Delta r)$ and (z, r_1) pairs, the coefficients a_i and b_i are obtained by solving the following least-squares optimization problems:

$$\min_{a_0,\dots,a_n} \sum_{k=1}^{N} \left(\Delta r^{(k)} - \sum_{i=0}^{n} a_i (r_1^{(k)})^i \right)^2 , \tag{5}$$

and

$$\min_{b_0,\dots,b_n} \sum_{k=1}^{N} \left(r_1^{(k)} - \sum_{i=0}^{n} b_i (z^{(k)})^i \right)^2 . \tag{6}$$

To model the time-delay profile between the two receivers, for each reflector, we express the travel times of the two acoustic paths as:

$$t_1 = \frac{r_1}{c_{avg}}, \tag{7}$$

and

$$t_2 = \frac{r_2}{c_{avg}}, \tag{8}$$

where t_1 and t_2 represent the theoretical times of flight from the transmitter to the reflector and then to receivers R_1 and R_2, respectively. Here, c_{avg} is the average sound speed along the propagation path. Assuming a horizontally stratified ocean, the same c_{avg} is used for both ray paths.

The corresponding theoretical time-delay is defined as $\Delta t = t_2 - t_1$, which can be expressed as a nonlinear function of c_{avg} and t_1 by substituting equation (3) for Δr, and applying equations (7) and (8). This yields the following time-delay profile:

$$\Delta t = a_n c_{avg}^{n-1} t_1^n + a_{n-1} c_{avg}^{n-2} t_1^{n-1} + \cdots + a_1 t_1 + \frac{a_0}{c_{avg}}. \tag{9}$$

This equation defines the theoretical time-delay as a function of t_1 and c_{avg}, with the coefficients a_i determined using equation (5). For each time window, the average sound speed is estimated by minimizing the RMS error between the experimental and theoretical time-delay profiles. Here, a time window refers to a short segment of the experimental time-delay profile over which the average sound speed is estimated. The corresponding range r_1 is then calculated using equation (7), and the depth of the reflector is subsequently calculated via equation (4) using the fitted coefficients b_i.

We utilize a cross-correlation technique between the two received signals to derive an experimental time-delay profile from observations. To ensure clarity, the time-delay profile estimated using either experimental received signals or synthetic received signals will be referred to as the "experimental time-delay profile."

Let t_s represent the time between data samples, and consider a time-gate window of L samples used in the cross-correlation between received signals. The cross-correlation between the time-gate window of the signal received by R_1 at some sample number l, starting at time $l \cdot t_s$, and the time-gate window of the signal received by R_2 at sample number $(l+k)$, starting at time $(l+k) \cdot t_s$, is calculated as:

$$R[l,k] = \frac{\sum_{i=0}^{L-1} \left(S_1[l+i] \cdot {S_2}^*[l+k+i]\right)}{\sqrt{\sum_{i=0}^{L-1}(S_1[l+i])^2 \cdot \sum_{i=0}^{L-1}({S_2}^*[l+k+i])^2}}, \tag{10}$$

where S_1 and S_2 denote the signals received by R_1 and R_2, respectively. As a result of reflected signals from various discrete targets, distinctive peaks appear in $R[l,k]$, corresponding to the time delays t_1 and Δt linked with these targets. If a peak emerges at position (l_0, k_0) within the cross-correlation matrix, it implies that $l_0 \cdot t_s$ and $k_0 \cdot t_s$ represent potential t_1 and Δt for a given target in the experimental time-delay profile. By minimizing the RMS difference between the theoretical time-delay profile given by (9) and the experimental time-delay profile, we can estimate c_{avg}.

Our methodology considers that t_1 and t_2 correspond to the arrival times of individual targets. However, the inherent nature of cross-correlation in (10) introduces the possibility of cross-contamination among multiple targets. This cross-contamination appears as confounding peaks in the cross-correlation data. The arrival time t_1 of one reflector is mistakenly linked to the arrival time t_2 of another. These incorrect $(t_1, \Delta t)$ pairs lead to inaccurate sound speed estimations. To mitigate this contamination, we implement pulse repetitions and average the absolute value of the cross-correlation results as follows:

$$\bar{R}[l,k] = \frac{1}{N}\sum_{i=1}^{N} |R[l,k]|, \tag{11}$$

where N is the number of pulse repetitions. This averaged data allows incorrect peaks corresponding to wrong arrival time pairs to converge towards a low-level background correlation level. This phenomenon occurs because the correlation peaks associated with individual targets consistently appear in the same time-delay region, while unwanted peaks from multiple reflectors occur at random delay times. By averaging the absolute cross-correlations over multiple pulses, the unwanted peaks tend to cancel out, converging to a lower level. In contrast, the valid peaks add coherently, making the true time-delay profile more distinguishable. The results of the simulations presented in section IV demonstrate how averaging the absolute value of the cross-correlation can effectively mitigate the issue of cross-contamination among targets.

In addition to averaging the absolute cross-correlations, when conditions allow for clearly identifiable echoes, the experimental time-delay profile can be formed by selecting distinct and robust reflections from individual pulse transmissions.

III. Received Signal Model

The performance of the proposed technique has been explored using a simulation approach utilizing synthetic received signals. Ray theory is employed to model the received signals (see, for example, [21], [22]). Our approach to modeling the received signals involves utilizing the time-invariant model proposed by [23] and subsequently integrating the time variation of propagation into the model.

Assume that the transmitted pulse template is $p(t)$, and $S_i(t)$ is the received signal at the ith receiver. The received signals can be formulated as follows:

$$S_i(t) = \sum_{j=1}^{M} a_{ij}(t) p\left(t - \tau_{ij}(t)\right) + n_i(t), \quad i = 1, 2. \tag{12}$$

Here, M denotes the number of scatterers, $a_{ij}(t)$ and $\tau_{ij}(t)$ represent the amplitude fading and arrival time of the ray reflected from the jth scatterer and received by the ith receiver respectively; here $n_i(t)$ is the acoustic and electronic noise sum at ith receiver. The statistical properties of the $a_{ij}(t)$ and $\tau_{ij}(t)$ can be determined by time-invariant and time-variant analysis of the propagation.

Considering the time-invariant acoustic propagation channel and the geometry illustrated in Fig. 1, we calculate the distance r_{ij} traveled to the ith receiver by the eigenray associated with the

jth reflector at location (x_j, y_j, z_j). This distance is determined using (1) and (2). Subsequently, each ray has an arrival time given by:

$$\tau_{ij} = \frac{r_{ij}}{c_{avg_j}}, \quad i = 1, 2 \quad , \tag{13}$$

where c_{avg_j} denotes the average sound speed between the transducer level and the jth reflector. Assuming spherical spreading and accounting for absorption, a factor denoting the decrease in pressure amplitude along a ray of length r_{ij} is:

$$L(r_{ij}) = \frac{1}{r_{ij}} \times 10^{\left(\frac{-\alpha r_{ij}}{20}\right)}, \quad i = 1, 2 \quad , \tag{14}$$

where α represents the total absorption coefficient in dB/m, and we compute it using the empirical formula proposed in [24].

The basics of propagation presented above explain time-invariant acoustic propagation. However, successive backscatter experimental signals show a statistical variation in arrival time and amplitude which we allow for in the model. Each path's arrival time and amplitude are assumed to be random processes, and their statistical properties are determined by the transducer movements and inherent time-variance of propagation media.

We assume that the arrival time for each path depends on the horizontal and vertical displacements of the transducers. Hence, changes in arrival times are connected to the spatial displacement of transducers by the equation:

$$\Delta\tau_{ij} = \frac{\partial \tau_{ij}}{\partial h}\Delta h + \frac{\partial \tau_{ij}}{\partial d_i}\Delta d_i, \quad i = 1, 2. \tag{15}$$

Here, Δ represents the small change operator. Assume that Δh and Δd_i are independent Gaussian random variables with zero mean and variances of ${\sigma_h}^2$ and ${\sigma_{d_i}}^2$, respectively. Hence, according to equation (15), $\Delta\tau_{ij}$ is also a Gaussian random variable with zero mean and the variance:

$${\sigma_{\tau_{ij}}}^2 = \left|\frac{\partial \tau_{ij}}{\partial h}\right|^2 {\sigma_h}^2 + \left|\frac{\partial \tau_{ij}}{\partial d_i}\right|^2 {\sigma_{d_i}}^2, \quad i = 1, 2. \tag{16}$$

Combining Eqs. (1), (2), and (13), we obtain:

$$\frac{\partial \tau_{ij}}{\partial h} = \frac{1}{c_{avg_j}} \left(\frac{-z_j}{\sqrt{x_j^2 + y_j^2 + z_j^2}} + \frac{-z_j}{\sqrt{(x_j - d_i)^2 + y_j^2 + z_j^2}} \right), \quad i = 1, 2 \ , \tag{17}$$

and

$$\frac{\partial \tau_{ij}}{\partial d_i} = \frac{-1}{c_{avg_j}} \left(\frac{x_j - d_i}{\sqrt{(x_j - d_i)^2 + y_j^2 + z_j^2}} \right), \quad i = 1, 2. \tag{18}$$

Combining the time-invariant and time-variant component together, for each scatterer, $\tau_{ij}(t)$ follows a Gaussian process with mean value and variance determined by (13) and (16), respectively.

Amplitude fading, $a_{ij}(t)$ in (12), is a well-studied characteristic, and literature presents theoretical and experimental evidence supporting Rayleigh or Ricean distributions for amplitude fading of individual rays [23], [25]–[27]. In our study, we adopt a Rayleigh distribution for the amplitude fading of successive eigenrays. Thus, according to the time-invariant analysis of the propagation, the amplitude $a_{ij}(t)$ in (12) is modeled as a Rayleigh process with mean value:

$$\mu_{a_{ij}} = b_T(\theta_{T_j}) b_{R_i}(\theta_{R_{ij}}) L(r_{ij}), \quad i = 1, 2. \tag{19}$$

Here, $b_T(\theta_{T_j})$ and $b_R(\theta_{R_{ij}})$ denote the transmitter and receiver beam pattern amplitudes for the jth scatterer in the transmission and receiving directions of θ_{T_j} and $\theta_{R_{ij}}$, respectively.

In order to use (12) and (13) for modeling the received signals, we have to consider the average sound speed for each eigenray. Assuming the SSP is known, we utilize the model presented in [14] to find the average sound speed for each reflector. This model, depicted in Fig. 2, illustrates equally spaced layered media with a reflector located at the $(N+1)$th layer. For the ray connecting the transmitter to the reflector, the following relationship holds:

$$\tau = \sum_{i=1}^{N} \Delta\tau_i + \delta\tau, \tag{20}$$

where τ represents the time of flight between the transmitter and reflector, while $\Delta\tau_i$ and $\delta\tau$ denote the time of flight in the ith and last layer, respectively. As the time of flight τ can be calculated as the distance between transmitter and reflector divided by average sound speed, (20) gives:

$$\frac{N\Delta d + \delta d}{c_{avg}} = \sum_{i=1}^{N} \left(\frac{\Delta d}{c_i} \right) + \frac{\delta d}{c_{N+1}}, \tag{21}$$

where Δd is the ray length in each layer, and δd is the ray length in the last layer. Using (21), the average sound speed can be expressed as:

$$c_{avg} = \frac{N + \frac{\delta d}{\Delta d}}{\sum_{i=1}^{N} \frac{1}{c_i} + \frac{\frac{\delta d}{\Delta d}}{c_{N+1}}}. \tag{22}$$

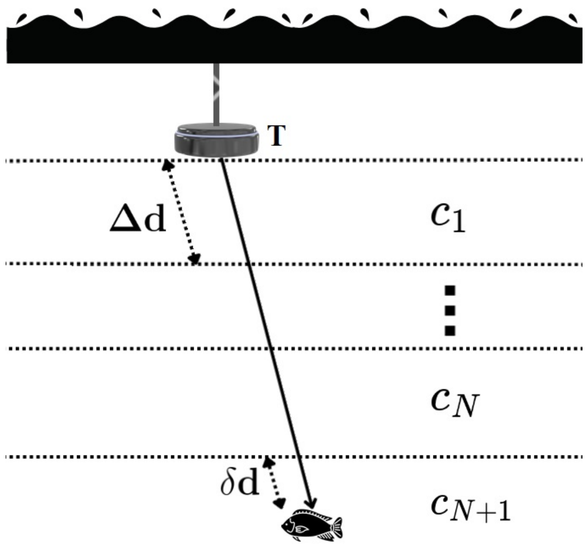

Fig. 2: Geometry of layered media with a local sound speed in each layer.

In a layered ocean, assuming horizontal uniformity in sound speed and that receivers and transmitter are at the same depths, the average sound speed for the transmitter-reflector ray and reflector-receiver ray are equal, and c_{avg} determined from (22) represents the average sound speed for the entire ray path from the transducer to the reflector and then to the receiver.

The interval velocity between two reflectors at depths z_j and z_{j-1} is determined using the estimated average sound speed, c_{avg}, at these depths through the following equation:

$$c_j = \frac{z_j - z_{j-1}}{\frac{z_j}{c_{avg_j}} - \frac{z_{j-1}}{c_{avg_{j-1}}}} \tag{23}$$

The final SSP is estimated from this series of c_j values.

IV. Results and Comparisons

To estimate the sound speeds using the theoretical time-delay profile and to calculate reflector depths, the determination of the coefficients a_i and b_i in (3) and (4) is necessary. For this purpose, taking into account the location and beamwidth of the transducers, the method presented in section II is used. For example, assume a transmitter positioned at the origin, with two receivers aligned along the x-axis at distances $d_1 = 10$ m and $d_2 = 12$ m, respectively. Considering a 3 dB beam pattern of 7 degrees for the transmitter, exploration of the SSP up to a depth of 150 m is conducted.

The relationship between Δr and r_1, as well as r_1 and z, is assumed to fit polynomials of degree 6. This degree was chosen because increasing it further does not improve the least squares fit. Random reflector locations are distributed within a cone originating from the transmitter, with a density of 10 reflectors per cubic meter $(1/\mathrm{m}^3)$. The cone's angle is half the transmitter's 3 dB beam width. Utilizing (1) and (2), the values of $(r_1, \Delta r)$ and (z, r_1) for these reflectors are computed. Subsequently, the coefficients a_i and b_i in (3) and (4) are determined by applying a least-squares curve fitting technique from Eqs.(5) and (6). An example of this process is illustrated in Fig. 3, which shows the polynomial fit for $(r_1, \Delta r)$ data, with the resulting fit used to determine a_i. The corresponding coefficients a_i and b_i, obtained from the least-squares fitting

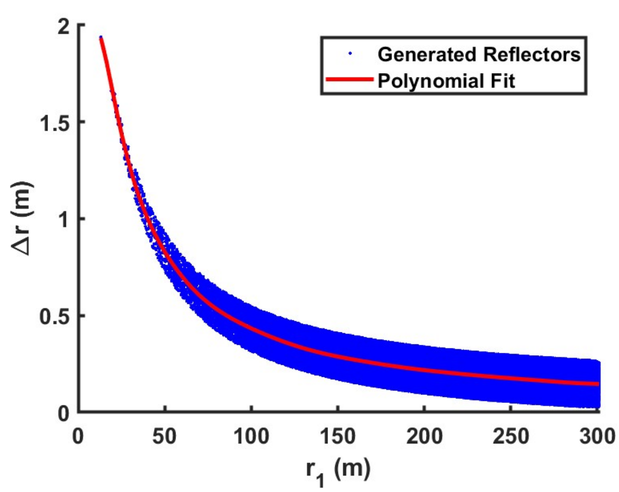

Fig. 3: Variations in ray lengths plotted against the ray length received by R_1, with a polynomial fit (n=6).

procedure, are listed in Table I.

TABLE I: Estimated polynomial coefficients a_i and b_i from the least-squares fits.

Index	a_i	b_i
a_6, b_6	5.63×10^{-14}	1.46×10^{-11}
a_5, b_5	-6.39×10^{-11}	-8.04×10^{-9}
a_4, b_4	2.94×10^{-8}	1.78×10^{-6}
a_3, b_3	-7.05×10^{-6}	-2.04×10^{-4}
a_2, b_2	9.45×10^{-4}	1.28×10^{-2}
a_1, b_1	-7.03×10^{-2}	1.57×10^{0}
a_0, b_0	2.71×10^{0}	7.35×10^{0}

To validate the presented method, synthetic received signals are generated as described in section III. These signals are used to derive the experimental time-delay profile and estimate the SSP. The parameters used in the simulations are summarized in Table II. When specific parameters are adjusted, the corresponding changes are noted in the relevant sections. The transducer displacements reported in Table II correspond to the variations per ping in the position of the transducer between transmission and reception. In practical deployments, transducers are typically mounted on a rigid frame, causing the entire array to move as a single body due to platform motion. In such cases, the relative geometry between the transducers remains unchanged, and this ping-to-ping motion can be accurately tracked using onboard motion sensors, such as an inertial measurement unit (IMU). The measured motion data can then be used to adjust the estimated SSP for each ping, compensating for platform-induced bias.

The simulation results are presented in two stages. First, the steps for estimating the depth-dependent SSP are demonstrated using the pulse repetition method. Then, to analyze factors influencing SSP estimation, a constant sound speed of 1520 m/s is assumed between the sea surface and a depth of 50 m. This assumption isolates the technique's limiting performance under controlled conditions. The focus on depths less than 50 m ensures computational efficiency while addressing the ocean's most dynamic region, where significant sound speed variations occur. Factors such as transmit pulse length, reflector density, signal-to-noise ratio (SNR), transducer geometry, depth, and the transmitter's 3 dB beam width are investigated.

TABLE II: Parameters Used for Simulation

Parameter	**Value**	**Units**
h	0	m
d_1	10	m
d_2	12	m
Center frequency	100	kHz
Sampling frequency	400	kHz
Time window for sound speed estimation	1	ms
Pulse length	1.5×10^{-4}	s
Vertical transducer RMS movement	0.1	m
Horizontal transducer RMS movement	0.02	m
Signal-to-Noise Ratio (SNR)	20	dB
Density of reflectors	1	$1/\mathrm{m}^3$
3 dB beam width	7	degrees
Number of pulse repetitions	300	-
Degree of polynomial	6	-

A. SSP Estimation Procedure and the Effect of Pulse Repetition

To evaluate the benefit of pulse repetition on the accuracy of sound speed estimation, the number of repeated pulses in the simulation is varied and the effect of that on the SSP estimation is analyzed.

Fig. 4 illustrates the average sound speed estimation progression with pulse repetitions 10, 100, and 500. As expected, increasing the number of pulse transmissions and averaging over the absolute value of the cross-correlations leads to a reduction in the standard deviation of the estimated sound speed. This simulation results verify how averaging the cross-correlation's absolute value mitigates the cross-contamination among targets, as discussed in section II. As shown in Fig. 4, SSP estimation errors are greater near the surface due to the narrow beamwidth of the transmitter, which limits the insonified volume at shallow depths and reduces the number of available reflectors.

Further analysis is presented in Fig.5(a), which shows the standard deviation of the estimated average sound speed relative to the assumed value of 1520 m/s (between 0 and 50 m) as a function of pulse repetitions. As expected, the estimation standard deviation will decrease as more pulse repetitions are used. Fig. 5(b) shows the progression in estimated average sound speed after 30, 120, and 200 pulse repetitions.

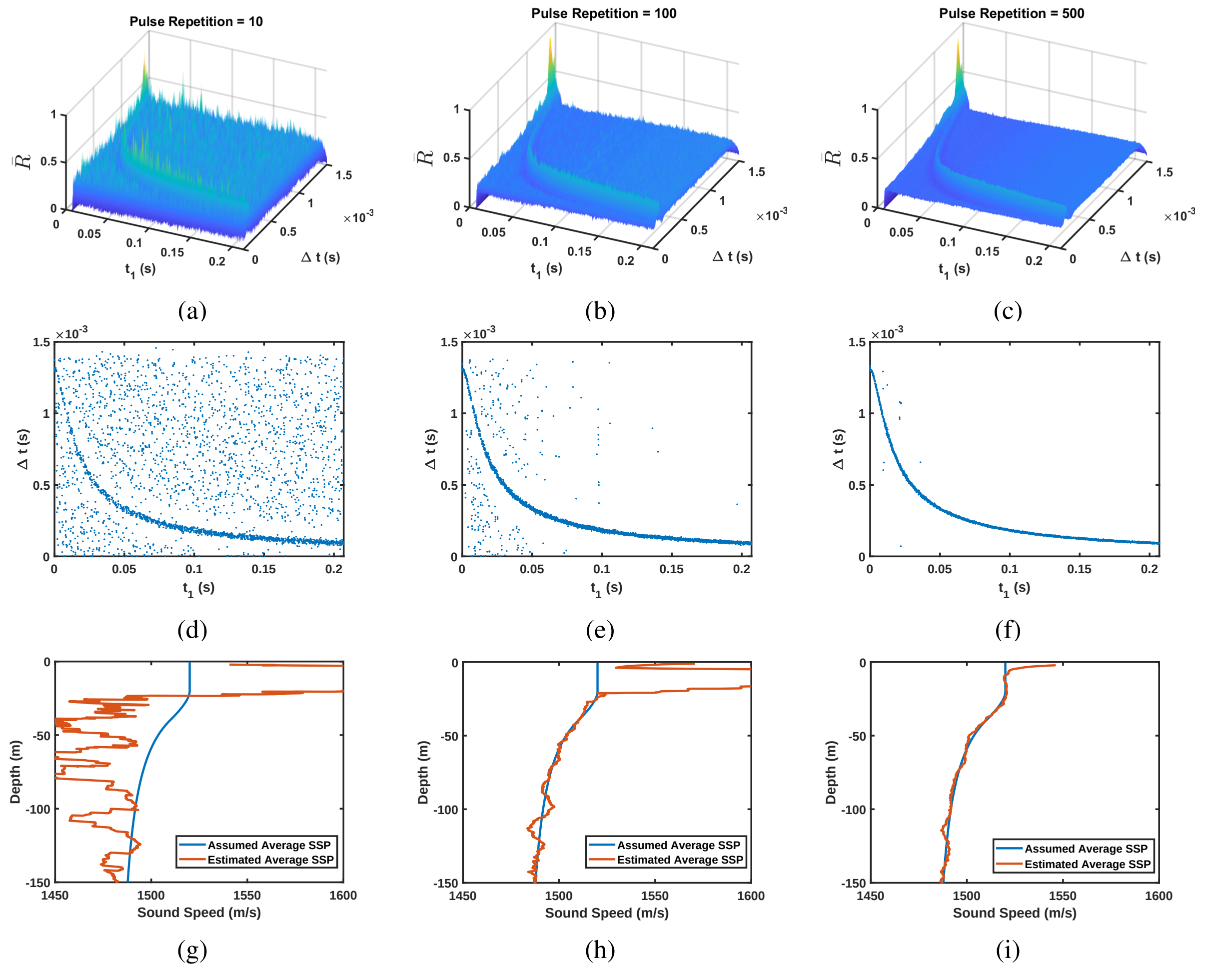

Fig. 4: (a)–(c) show $\bar{R}$ for three representative cases. (d)–(f) present the corresponding Δt values associated with the maximum of $\bar{R}$ for each t_1 (experimental time-delay profiles). (g)–(i) display the estimated average sound speed profiles for each case.

B. *Effect of Pulse Length on SSP Estimation*

Transmit pulse length directly influences the estimation of the experimental time delay profile in conjunction with the density of the reflector. Assuming a reflector density of 1 $(1/\mathrm{m}^3)$, Fig. 6(a) illustrates the standard deviation of the estimated average sound speed relative to the assumed value of 1520 m/s, as a function of pulse lengths. Additionally, Fig. 6(b) shows the estimated average sound speed using pulse lengths of 0.04, 0.15, and 7.4 ms. According to Fig. 6(a), there exists a pulse length interval that minimizes the standard deviation to less than 5 m/s. The lower boundary is approximately 0.05 ms, which corresponds to five cycles of the transmit

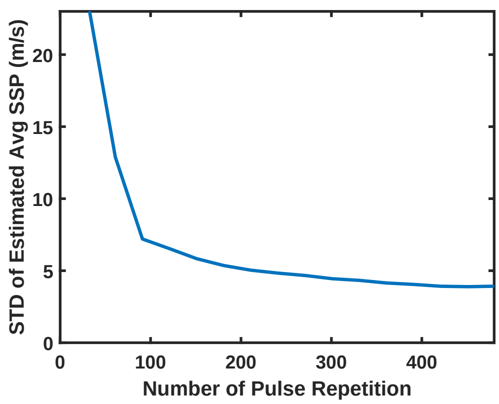

(a)

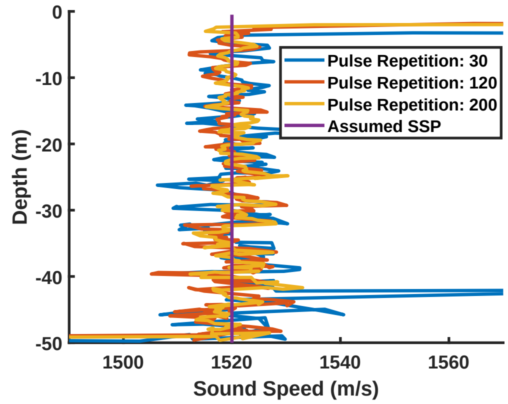

(b)

Fig. 5: (a) The standard deviation of the estimated average sound speed as a function of pulse repetitions. (b) Estimated average sound speed corresponds to 30, 120, and 200 pulse repetitions.

pulse, while the upper boundary of pulse length is around 1.4 ms. Using shorter or longer pulse lengths increases the standard deviation.

When applying the cross-correlation process in (10) to estimate t_1 and Δt, shorter pulses (less than 0.05 ms) contain fewer data samples and less power, making it difficult for the correlation process to accurately match replicas and determine t_1 and Δt. Conversely, longer pulse lengths also present challenges when echo signals start blending together or becoming indistinguishable. This problem becomes more evident at greater depths where the 3 dB beam width of transducers covers a larger area and encounters more reflectors. This overlap restricts the ability to estimate t_1 and Δt and the experimental time-delay profile. Achieving a balance between providing sufficient echo duration for correlation and avoiding excessive pulse lengths is essential, especially in environments with higher reflector densities.

C. Effect of Reflector Density on SSP Estimation

The performance of the proposed sound speed estimation method relies on the presence of reflectors within the ocean column. The density of such reflectors directly influences the reliability of the received acoustic signals. In practice, the distribution of reflectors can vary significantly with location, time, and depth. This sensitivity to the reflectors is similar to Acoustic Doppler Current Profilers (ADCPs), which also depend on volume backscatter to estimate current

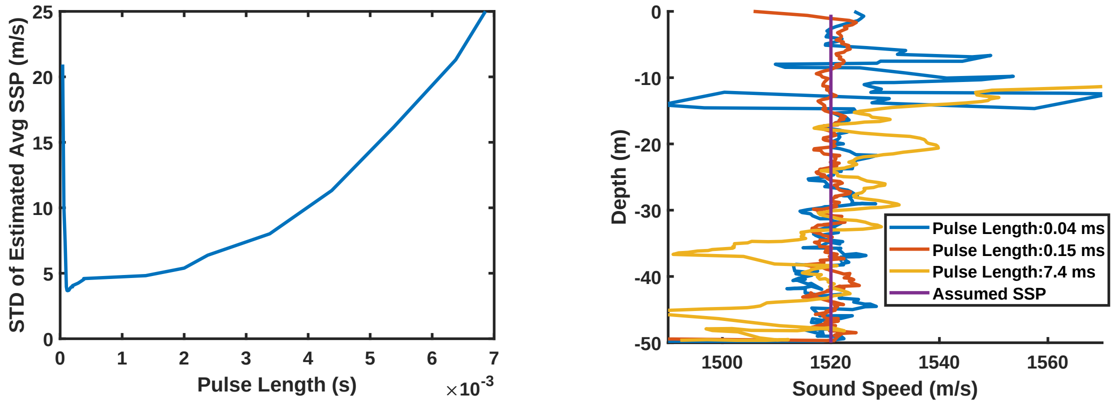

(a) (b)

Fig. 6: (a) The standard deviation of the estimated average sound speed as a function of pulse length. (b) The estimated average sound speed corresponds to 0.04 ms, 0.15 ms, and 7.4 ms pulse length.

velocities at various depths [28]. To assess this dependence, we varied the spatial density of the simulated reflectors in the ocean column and measured their impact on the accuracy of the estimation.

Assuming a pulse length of 0.15 ms, Fig. 7(a) illustrates the standard deviation of the estimated average sound speed relative to the assumed value of 1520 m/s as a function of reflector density. Fig. 7(b) displays the estimated average sound speed for reflector densities of 1.25, 3, and 5 ($1/\mathrm{m}^3$). Based on the observations from Fig. 6(a) and Fig. 7(a), it is evident that the minimum standard deviation values for different pulse lengths and reflector density occur in a bounded region with the lower and upper limits depending on interaction between both factors. Similarly to the effect observed with increasing pulse length, a higher reflector density causes the echoes from individual reflectors to blend, making it difficult, or even impossible, to accurately estimate the experimental time-delay profile.

D. Effect of SNR on SSP Estimation

The performance of the method is evaluated under varying signal-to-noise ratios. We define SNR as the ratio of the RMS values of the received echo signal from a single reflector to that of normally distributed noise introduced into the received signals. As SNR decreases, noise

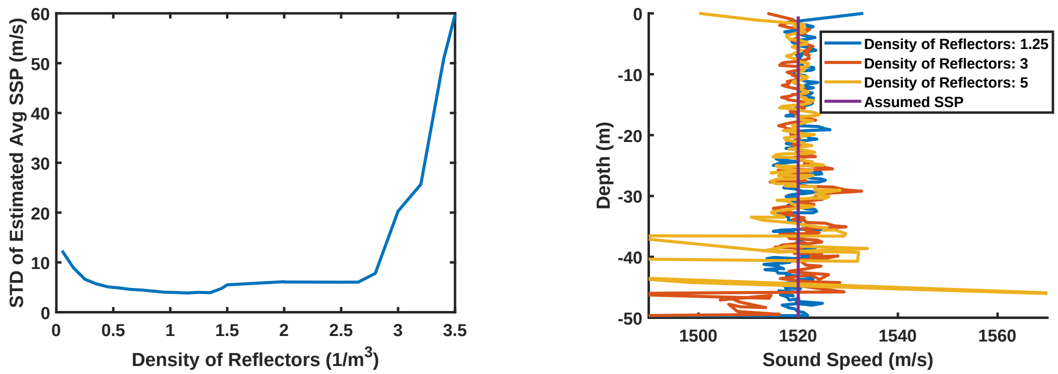

(a) (b)

Fig. 7: (a) The standard deviation of the estimated average sound speed as a function of reflector density. (b) Estimated average sound speed corresponds to 1.25, 3, and 5 $(1/\mathrm{m}^3)$ reflector density.

begins to dominate the signal waveform, which negatively affects the accuracy of the cross-correlation process in equation (10). This temporal uncertainty caused by noise can result in errors in estimating the experimental time-delay profile, and consequently, the estimated sound speed profile.

Fig. 8(a) shows that when the SNR exceeds approximately 12 dB, the standard deviation of the estimated average sound speed remains below 5 m/s, indicating acceptable estimation stability. Below this threshold, performance degrades rapidly due to poor correlation between noisy echoes at two receivers. Fig. 8(b) presents the estimated average sound speed for SNR values of -2.5, 6.5, and 12 dB, illustrating this transition from unstable to stable estimation.

E. Effect of Transducer Geometry on SSP Estimation

Another parameter that influences system performance is the overall size of the setup, characterized by the distance between the transmitter and the second receiver. Assuming a constant distance between receivers of 2 meters, Fig. 9(a) displays the standard deviation of the estimated average sound speed as a function of d_1, the distance from the transmitter to the first receiver. As d_1 increases, the standard deviation decreases, reflecting improved estimation accuracy. This progression can also be seen by estimated profiles shown in Fig. 9(b).

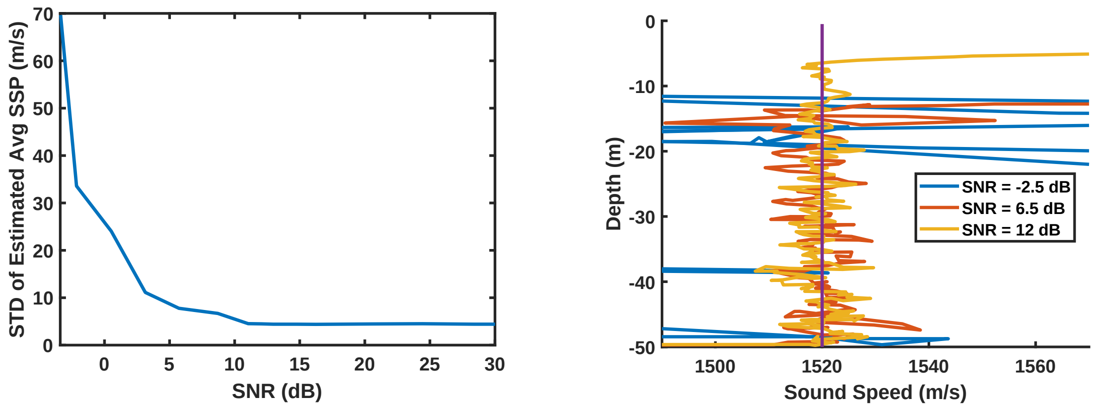

(a) (b)

Fig. 8: (a) The standard deviation of the estimated average sound speed as a function of SNR. (b) Estimated average sound speed corresponds to SNR of -2.5 dB, 6.5 dB, and 12 dB.

Given the constant distance between the two receivers, the dependence of the standard deviation on d_1 can be understood by examining the relationship between arrival time delay, Δt, and average sound speed. Similar to the theoretical time-delay profile described by (9), we express Δt as a function of c_{avg} and t_1 as $\Delta t = f(c_{avg}, t_1)$. The error in Δt can then be related to errors in c_{avg} and t_1 through the following relationship:

$$\delta \Delta t = \frac{\partial \Delta t}{\partial c_{avg}} \delta c_{avg} + \frac{\partial \Delta t}{\partial t_1} \delta t_1 \tag{24}$$

here, $\delta(\cdot)$ represents the error in a parameter. Given $c_{avg} = r_1/t_1$ and $c_{avg} = \Delta r/\Delta t$, and with the assumption that $t_1 >> \Delta t$, we derive:

$$\delta c_{avg} = \frac{c_{avg}}{\Delta t} \delta \Delta t. \tag{25}$$

As the receivers are placed farther from the transmitter, the ray length difference Δr and so Δt increase. Assuming that the error in estimating the arrival time differences remains constant for different d_1 values, (25) shows that an increase in Δt reduces the error in estimating the average sound speed. This trend is consistent with the results presented in Fig. 9, demonstrating the benefits of larger transmitter-receiver spacing for sound speed estimation accuracy.

Next, consider a case where the second receiver is fixed at $d_2 = 20$ m. Fig. 10(a) demon-

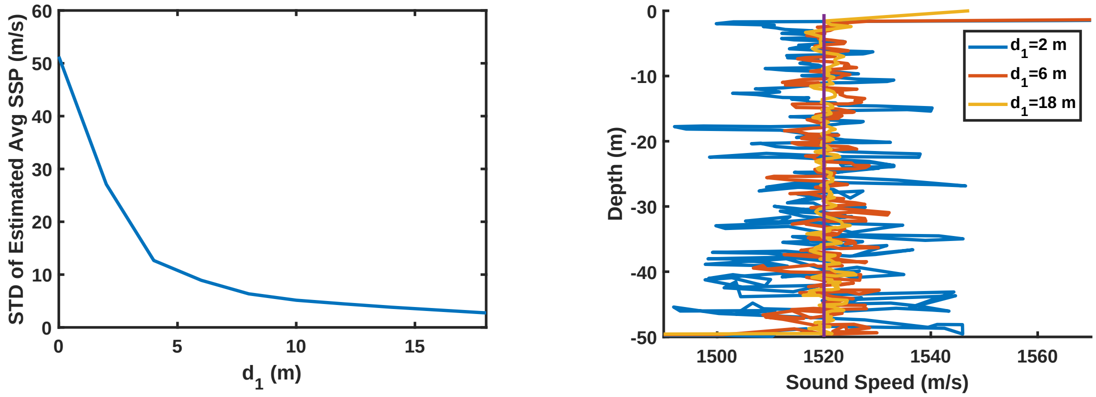

(a) (b)

Fig. 9: (a) The standard deviation of the estimated average sound speed as a function of d_1 while maintaining $d_2 = (d_1 + 2)$m. (b) Estimated average sound speed for different values of $d_1 = 2, 6,$ and 18 m, with $d_2 = (d_1 + 2)$m.

strates how the standard deviation of the estimated average sound speed changes with different locations of the first receiver, d_1. Fig. 10(b) shows the estimated average sound speed for $d_1 =$ 14, 16, 18 m. The results show that the standard deviation decreases as the first receiver approaches the second, reaching a minimum at a separation of approximately 2 meters, contrary to the expectation from (25).

This unexpected finding can be better understood by examining Figs. 11 and 12. For a constant sound speed of 1520 m/s up to 50 m depth, random reflector locations were generated within a transmitted beam with a 3 dB beamwidth of 7 degrees. Fig. 11(a) shows the time-delay pairs for these reflector locations when the second receiver is located at $d_2 = 20$ m and $d_1 = 8, 12, 18$ m. Fig. 11(b) shows the time-delay pairs for a fixed receiver spacing of 2 meters at the same d_1 positions considered in Fig. 11(a).

In contrast to the case with constant receiver spacing (Fig.11(b)), increasing the separation between receivers significantly expands the range of Δt values for each t_1 (Fig.11(a)). For example, at $d_1 = 18$ m$, d_2 = 20$ m, the Δt range at large t_1 is approximately one pulse length (0.15 ms), while for $d_1 = 8$ m$, d_2 = 20$ m, it expands to nine pulse lengths. For geometries with a large Δt range relative to the pulse length, cross-correlation peaks become more separated, reducing the average correlation peak height relative to the background correlation level in $\bar{R}$.

Conversely, in scenarios where the Δt range is comparable to or smaller than the pulse length, the correlation peaks from reflectors overlap constructively in $\bar{R}$, increasing the average peak height.

Fig. 12 provides further insights where Fig. 12(a) and (b) show the contours of $\bar{R}$ for longer and shorter receivers separations, respectively, while Fig. 12(c) and (d) show the corresponding maximum $\bar{R}$ for each t_1. The poorly defined peaks in Fig. 12(a) introduce uncertainty in the estimation of Δt as shown by the increased scatter observed in Fig. 12(c). Consequently, $\delta\Delta t$ cannot be assumed constant in (25); instead, the increasing $\delta\Delta t$ exceeds any benefit resulting from an increase in Δt.

Returning to Fig. 10, the improvement in results with reduced separation has a limit. When the receivers are positioned too closely together, the standard deviation of the estimated sound speed begins to increase. This occurs because, with a smaller separation, the time difference between the arrivals of echoes at the two receivers diminishes, potentially falling within the pulse length. In this scenario, as the receivers are brought closer together, Δt decreases while $\delta\Delta t$ remains constant, leading to an increase in the standard deviation of the estimated sound speed, as indicated by (25). From the perspective of pulse length, using short pulses relative to the expected range of Δt yields similar results, wherein the correlation outcomes of the reflectors do not contribute constructively to the average value of the absolute cross-correlation.

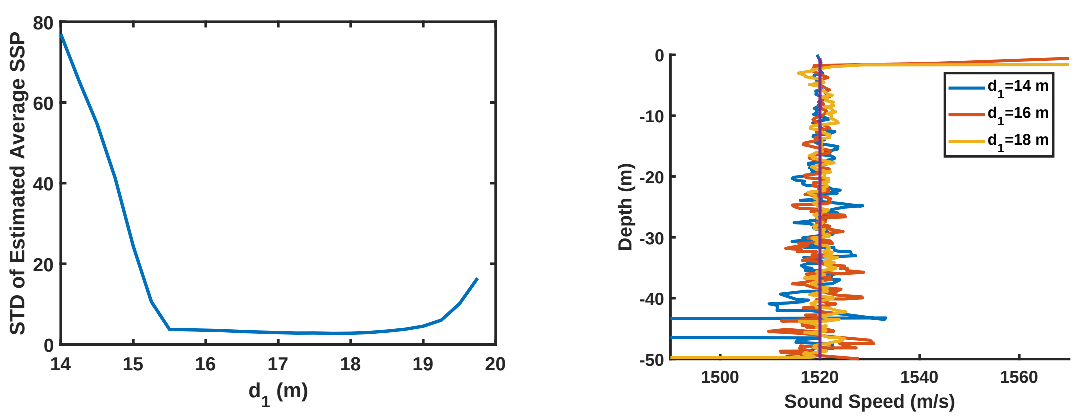

(a) (b)

Fig. 10: (a) The standard deviation of the estimated average sound speed as a function of d_1 when $d_2 = 20$ m. (b) Estimated average sound speed for $d_1 = 14$, 16, 18 m, when $d_2 = 20$ m.

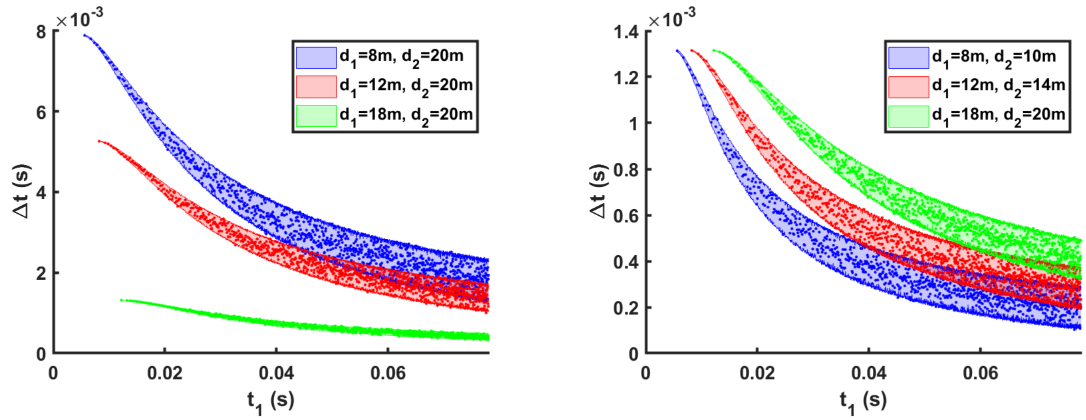

(a) (b)

Fig. 11: Illustration of time delay pairs for reflector locations within the transmitted beam. The plot demonstrates the distribution of time delays (a) as the distance between receivers increases when $d_2 = 20$ m, and (b) as the distance between the transmitter and the first receiver increases when $d_2 = (d_1 + 2)$ m.

F. Depth-Dependent Effects on SSP Estimation

To evaluate how depth-related parameters influence the accuracy of sound speed estimation, both the effect of reflector depth and the transmitter's 3 dB beam width were analyzed. To investigate how the proposed method performs at different depths, we fixed the transmitter and receivers at positions $d_1 = 20$ m and $d_2 = 22$ m, respectively, with a constant sound speed of 1520 m/s to a depth of 200 m. Fig. 13(a) illustrates the estimated average sound speed profile, and Fig.13(b) displays the standard deviation of the estimated average sound speed relative to the assumed value, calculated within non-overlapping 5-meter depth intervals. The standard deviation increases with depth due to the wider coverage of the transducers' 3 dB beam width, resulting in more reflectors and more blending of reflections over the duration of the pulse. Additionally, the deeper part of the ocean results in smaller Δt leading to larger errors in average sound speed (see equation (25)).

The standard deviation of the estimated average sound speed relative to 1520 m/s for different 3 dB beam widths of the transmitter is shown in Fig. 14. As the 3 dB beam width of the transmitter increases, the standard deviation of the estimated sound speed also increases. This trend can be attributed to more reflectors within the larger beam coverage area and the expanding

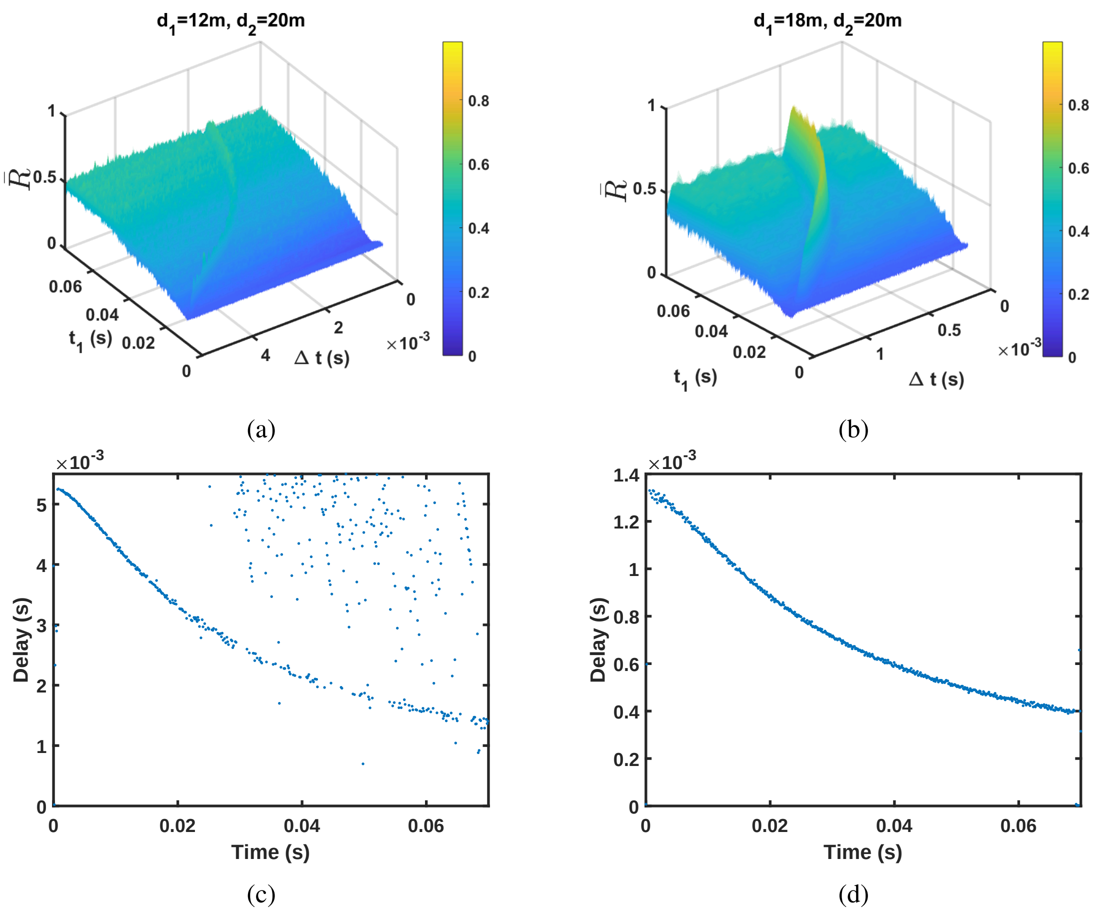

Fig. 12: The $\bar{R}$ and the experimental time-delay profiles are shown for two cases: with $d_1 = 12$ m and $d_2 = 20$ m in the left column, and $d_1 = 18$ m and $d_2 = 20$ m in the right column.

time-delay profile along Δt. Both factors contribute to a reduction in the average peak relative to the background correlation level in $\bar{R}$.

G. Deriving of the SSP from Average SSP

To derive the SSP from the averaged SSP, we can refer to equation (23). Assuming infinitesimally thin layers, this equation yields the following derivative relationship between SSP and average SSP:

$$\frac{1}{c(z)} = \frac{d}{dz}\left(\frac{z}{c_{avg}(z)}\right) \tag{26}$$

Considering $d_1 = 20$ m and $d_2 = 22$ m, along with 2000 pulse repetitions, Fig. 15(a) and (b) illustrate the estimated average SSP and SSP, respectively. Applying differentiation in (26)

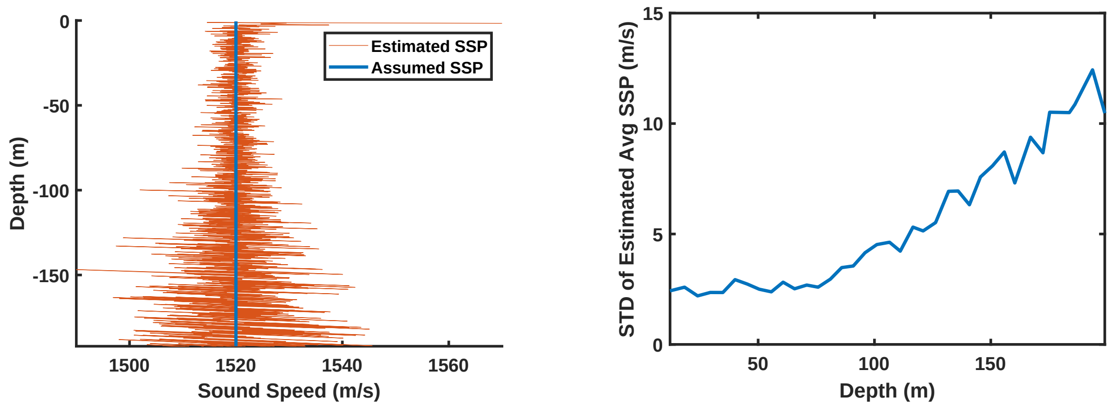

(a) (b)

Fig. 13: (a) Estimated average sound speed as a function of depth. (b) The standard deviation as a function of depth.

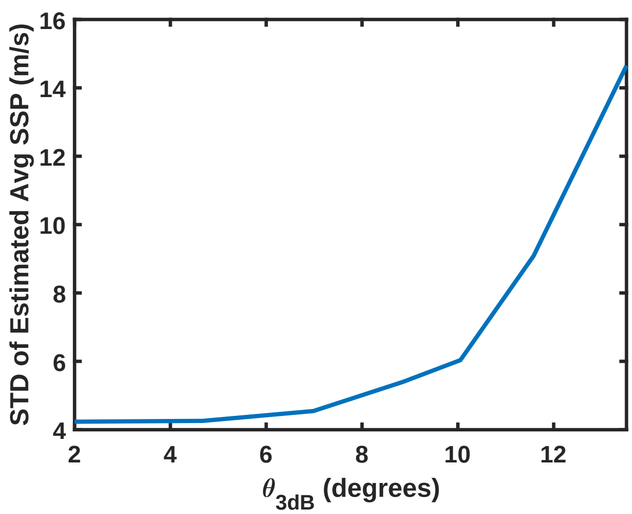

Fig. 14: The standard deviation of the estimated average sound speed as a function of the 3 dB beam width of the transmitter.

amplifies noise in our estimated SSP. Given that our estimated average SSP inherently contains noise, it becomes necessary to employ a large number of pulse repetitions and apply smoothing techniques to the estimated average SSP.

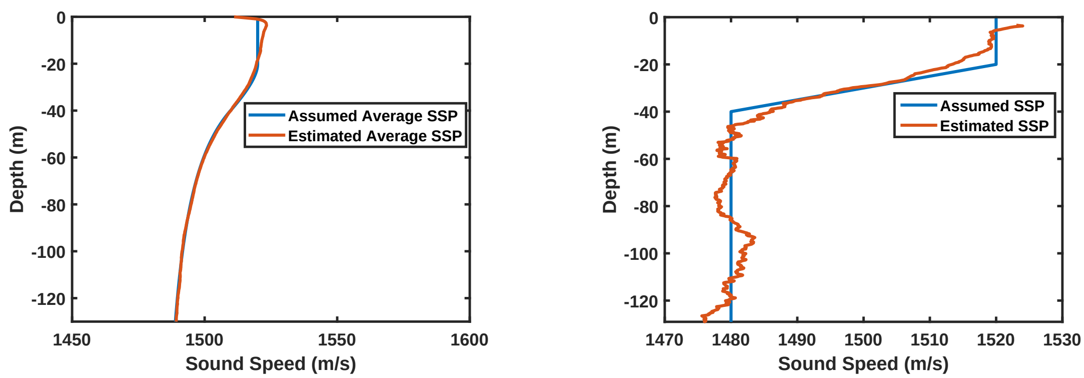

(a) (b)

Fig. 15: (a) Average SSP estimation. (b) SSP estimation.

V. Tank Test Experiment

To validate the presented method, we conducted an experiment in the National Research Council of Canada (NRC) towing tank. The tank is 200 m long, 12 m wide and 7 m deep, filled with fresh water at a nearly uniform temperature of 17.9°C. This temperature corresponds to an expected sound speed of 1475.6 m/s, calculated using the empirical formula for freshwater [29]:

$$c = 1404.3 + 4.7T - 0.04T^2, \tag{27}$$

where T is in degrees Celsius and c is in m/s.

Fig. 16 illustrates the experimental setup, including the transducer array, suspended reflectors, surface wave generator, and the overall layout within the tank.

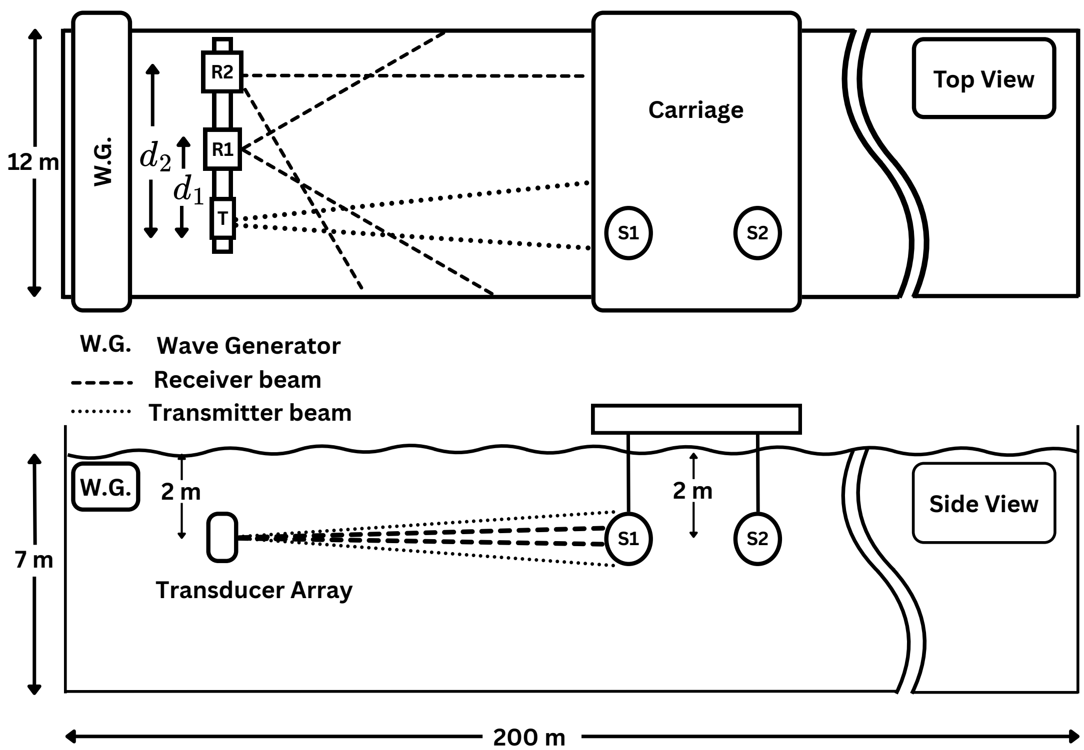

Fig. 16: Experimental setup geometry. The figure includes both a top view and a side view of the configuration. In the diagram, T denotes the transmitter, R1 and R2 represent the first and second receivers, respectively, and S1 and S2 indicate the suspended reflectors used in the experiment. The W.G. label in the figure refers to the surface wave generator.

We used a Furuno DFF3-UHD unit and a CA82B-35R transducer with a beam width of approximately 9 degrees as transmitter. Two side-scan sonar transducers were used to record the reflected signals. These side-scan transducers have a beam pattern with a wide 50-degree beam in one direction and a narrow 2-degree beam in the orthogonal direction. All transducers were mounted on a rigid aluminum beam, horizontally deployed at a depth of 2 m across the width of the tank. The distances between the transmitter and the receivers are 0.33 m and 7.39 m. The transmitter was tilted horizontally toward the interior of the tank by 2 degrees to minimize reflections from the close boundary of the tank. The first receiver did not have any tilt and the second receiver was tilted by 25 degrees toward the interior of the tank to align with the expected echo path. The side-scan transducers were mounted vertically on the aluminum beam, forming a cross-shaped configuration. In this orientation, they produced a beam pattern of 2 degrees vertical and 50 degrees horizontal within the tank.

Two spherical reflectors, a 6 cm diameter lead ball (S1) and a 15 cm diameter vinyl buoy (S2), were suspended from the overhead carriage at a depth of 2 m. The vinyl buoy was stabilized at this depth by a weight attached 4.5 m below it. Taking the transmitter as the origin, the reflectors were not aligned along the axis extending along the length of the tank. Instead, they were positioned approximately 25 cm laterally offset from this axis, on the side opposite the receivers, placing them closer to the tank wall than the transmitter. The horizontal separation between the two reflectors was approximately 15 m.

During the test, the initial distance between the first reflector and the transducer array was approximately 5 m. The carriage was then slowly moved along the length of the tank at a constant speed of 1 cm/s. This movement provided the necessary variation in reflector range to enable sound speed profile estimation, analogous to vertical profiling in ocean applications.

To suppress acoustic paths that interact with the water surface, waves were generated using the built-in wave generator of the tank. The waves had a height of 0.01 m and a period of 0.5 s. These small-amplitude surface perturbations broke up the otherwise mirror-like surface, reducing the coherence and strength of surface-reflected echoes through acoustic scattering. A comprehensive summary of the experimental setup and test conditions is provided in Table III.

Following the deployment of the transducer array and reflectors, signal recordings were made during the tank experiment. Although the transducers had narrow beam patterns and were tilted to mitigate both multipath effects and direct reflections from the boundaries, the tank environment

TABLE III: Experimental Setup Parameters

Parameter	Value	Units
Tank dimensions (L × W × D)	200 × 12 × 7	m
Water temperature	17.9	°C
Expected sound speed	1475.6	m/s
Transmitter model	Furuno CA82B-35R	-
Transmitter transducer tilt angle	3.57	degrees
Side-scan tilt angle (R1)	0	degrees
Side-scan tilt angle (R2)	25	degrees
Side-scan beamwidths	2 (H), 50 (V)	degrees
Transmitter-receiver distances	$d_1 = 0.33$, $d_2 = 7.39$	m
Deployment depth	2	m
Number of pulses	828	-
Center frequency	100	kHz
Sampling frequency	400	kHz
Pulse length	0.15	ms
Reflector types (Diameter)	Lead ball (6), Vinyl buoy (15)	cm
Carriage speed	1	cm/s
Surface wave height	0.01	m
Surface wave period	0.5	s

introduced persistent high acoustic interference throughout the recordings. This interference differed from typical ambient noise as it originated from strong repeated echoes reflecting off the tank boundaries and remained stable over time. As a result, cross-contamination occurred between the echoes of the two reflectors and the interference-induced echoes. Although this effect is somewhat similar to the impact of high reflector density described in Section IV, Part C, which can make estimation unreliable when the density is too high, these interference echoes do not originate from physical scatterers within the volume. Instead, they behave like reflector images created by stable multipath propagation, leading to numerous misleading peaks superimposed on a high background correlation level. Therefore, cross-correlation between received signals or averaging the cross-correlations between pulses, as described in equations (10) and (11), was not effective in extracting the experimental time-delay profile in this tank experiment.

To address the interference, the time-delay profile was instead extracted by selecting distinct and robust reflections. This process involved applying the Hilbert transform to the received signals and identifying high-amplitude echoes using an amplitude threshold. Among the detected echoes, only those associated with S1 and S2 were used for cross-correlation between receivers. High-amplitude interference echoes, which occurred at fixed times across all pulses, were excluded from delay estimation. Using the resulting experimental time-delay profile and the corresponding theoretical profile, the sound speed profile was determined over the range of reflector positions covered during carriage movement.

Fig. 17 presents the smoothed experimental time-delay profile along with the theoretical profile computed according to equation (9), assuming a constant sound speed of 1475.6 m/s. Fig. 18 shows the estimated sound speed profile compared with the theoretical sound speed derived from equation (27).

According to Fig. 18, the estimated sound speed profile shows a negative bias relative to the theoretical value. A likely cause of this deviation is the geometric mismatch between the actual reflector positions and the assumption used in the theoretical time-delay model. The model assumes that reflectors are distributed around the axis extending from the transmitter along the length of the tank, whereas the experimental reflectors were laterally offset by approximately 25 cm from this axis, on the side opposite the receivers. This offset resulted in longer acoustic travel paths. When these longer measured delays are compared with shorter theoretical path predictions, the proposed method leads to a bias toward lower sound speed estimates. Due to this lateral offset, the experimental delays are generally greater than those predicted by the theoretical model, as shown in Fig.17. Note that a positive bias would occur for targets that were located symmetrically on the other side of the transmitter axis, as the experimental travel paths become shorter than those assumed in the theoretical time-delay model.

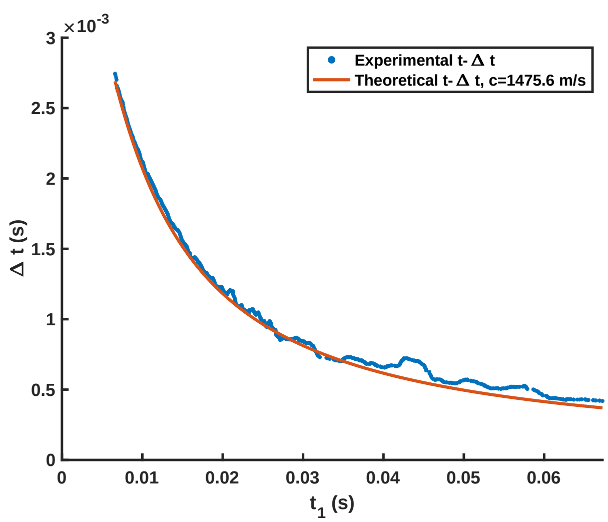

Fig. 17: Experimental and Theoretical time-delay profile with assuming c=1475.6 m/s.

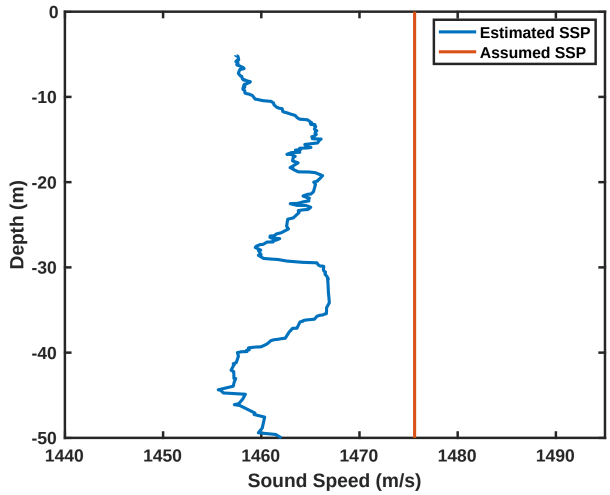

Fig. 18: Estimated sound speed profile in the tank compared with the theoretical sound speed calculated using equation (27). The estimated average SSP exhibited a negative bias of 14.01 m/s relative to the theoretical value, with a standard deviation of 3.23 m/s.

VI. CONCLUSION

We have introduced a bistatic pulse-echo method for remotely measuring ocean sound speed profiles. The fundamental setup includes a single vertically directed projector paired with two or potentially more horizontally displaced receivers (see Fig. 1). The presented approach does not need a large array compared to the sampled depth. It estimates the average sound speed between transducers and scatterers, enabling the determination of scatterers' depth and then SSP. This average sound speed is computed by minimizing the RMS difference between the experimental and theoretical time-delay profiles of echoes.

Evaluation of the method involved generating simulated received signals using a sound scattering model that considers sample geometry and propagation statistical properties. Time-delay profiles were generated by cross-correlating the simulated signals at two receivers, allowing us to identify travel times (t_1) and time differences (Δt) associated with discrete reflectors.

Two factors affect the accuracy of the cross-correlation process: Cross-contamination among reflectors can lead to correlation peaks where t_1 and Δt are derived from echoes associated with different reflectors, rather than a single target; second, there is echo blending, where echoes from different reflectors merge. To address cross-contamination, we employed pulse repetitions and averaged the absolute value of the cross-correlation results (as shown in equation (11)). Additionally, positioning the receivers closer together minimizes the Δt range of reflectors, concentrating the cross-correlation peaks within a narrow range relative to the pulse length. The narrowed cross-correlation peaks make the time-delay profile more distinguishable from the background correlation level (see Figs.11 and 12). Employing a shorter pulse compared to the Δt range offers no advantage from this perspective. The minimum separation between receivers, determined by the cross-correlation process, requires the echo delay of each reflector to exceed the pulse length. As depicted in Fig. 10, by $d_2 = 20$ m, the standard deviation of estimated sound speed increases when $d_1 > 19$ m.

Echo blending, which can occur due to high reflector density, long pulse lengths, wide beam transducers, or greater depths, can also impact sound speed estimation. Shorter pulses and narrower beam transducers can mitigate this issue. Additionally, transmitting coded pulses helps reduce echo blending.

Employing distinct and robust echoes to determine the experimental time-delay profile is an effective strategy for tackling both cross-contamination of reflectors and echo blending, thereby reducing the number of pulse repetitions needed. In this scenario, we acquire $(t_1, \Delta t)$ pairs related to the most prominent echoes from each pulse transmission are directly extracted and used to form the experimental time-delay profile.

Whether using averaged cross-correlation or distinct echoes, the method relies on the presence of well-separated reflectors or reflector volumes. Consequently, the data acquisition time depends on the availability and distribution of these reflectors rather than the pulse repetition rate of the acoustic system. The availability and quality of the ocean reflectors vary with location, season, and environmental conditions. The presented method addresses this variability through adaptable design choices such as frequency selection, pulse length, transmit power, transducer geometry, and adjustable repetition rates. Such techniques are well-established in sonar applications, such as ADCPs [30].

In addition to the simulation results, such as the example in Fig. 15, which produced profiles extending to 125 m depth with RMS errors of 0.67 m/s for the averaged SSP and 2.1 m/s for the local SSP, the experimental results further demonstrate the validity of the proposed method. In the experimental tank evaluation, the estimated average SSP exhibited a standard deviation of 3.23 m/s. This test also highlights the sensitivity to geometric bias introduced by the lateral offset of reflectors, which resulted in an average SSP bias of -14.01 m/s relative to the theoretical value. Depending on their position relative to the profiling axis, the reflectors can introduce either a negative or positive bias in the estimated sound speed. This bias will be mitigated with a more uniform distribution of reflectors around the system axis. In addition, incorporating an extra pair of receivers on the opposite side of the transmitter would enable symmetric measurements and reduce the sensitivity to lateral offsets. A similar strategy was demonstrated in [9], where signals were collected from multiple angular positions to average out lateral bias.

Also, the presented method, while demonstrated with one transmitter and two receivers, has the potential to be generalized for use with multiple receivers, which could further enhance the performance of the method in measuring sound speed profile.

Acknowledgments

We are immensely grateful to Dr. Mahmood Karimi from the School of Electrical and Computer Engineering, Shiraz University, Iran, and Dr. Jeremy Dahl from the Department of Radiology, Stanford University, USA, for their invaluable feedback, which contributed to the development of this research.

Appendix

Evaluation of Straight-Line Approximation in Sound Speed Estimation

Based on ray tracing theory, if the sound speed in the ocean does not change along the ray paths, the sound propagates in straight lines. However, in the ocean, sound speed varies with depth, temperature, and salinity, which change over time and location. As a result, sound rays typically follow curved paths. In our analysis, illustrated in Fig. 1 and described by (1) and (2), we approximate these curved paths as straight lines, even when sound speed varies with depth. This appendix examines how this approximation impacts the accuracy of sound speed estimation.

To analyze the effect of bending, we assume that the sound speed changes linearly within a single layer. This approximation of a linear variation in sound speed is not only mathematically convenient but also serves as a reasonable simplification for many oceanographic scenarios. In practice, the sound speed profile in the ocean often consists of multiple layers, each of which can be approximated with constant gradients. By adopting this layered approach, the method can generalize to more complex sound speed profiles through piecewise-linear representations. Suppose the sound speed varies linearly with depth between z_1 and z_2. In this case, sound speed can be modeled as:

$$c(z) = c(z_1) + g(z - z_1), z_1 < z < z_2, \tag{28}$$

where g is the sound speed gradient, calculated as:

$$g = \frac{c_2 - c_1}{z_2 - z_1}. \tag{29}$$

Here, c_1 and c_2 are the sound speed at depth z_1 and z_2, respectively. According to Snell's law, the path can be traced using the following relationship [31]:

$$\frac{\cos\theta_1}{c_1} = \frac{\cos\theta_2}{c_2} = \frac{\cos\theta(z)}{c(z)}, \tag{30}$$

where θ_1 and θ_2 represent the grazing angles of the ray at depths z_1 and z_2, respectively. When the sound speed varies linearly with depth, the ray path follows a circular arc, with the radius of the arc given by [31]:

$$R = \frac{c(z)}{|g| \cos\theta(z)}. \tag{31}$$

Fig. 19 illustrates the propagation geometry for both straight-line and curved paths in depth-range coordinates. In this illustration, the straight line from (z_1, r_1) to (z_2, r_2) represents the ray path under a no-bending assumption, while the curved arrow illustrates a bending path. Let s denote the ray length, and s_{straight} and s_{curve} represent the lengths of the straight and curved rays, respectively. Similarly, let τ denote the ray travel time, with τ_{straight} and τ_{curve} representing the travel times for each path. Given that $c_{avg} = s_{curve}/\tau_{curve}$, the difference in sound speed estimation resulting from assuming straight-line propagation instead of curved propagation can be determined using the following relationship:

$$\Delta(c_{avg}) = \frac{\partial c_{avg}}{\partial s_{curve}} \Delta s + \frac{\partial c_{avg}}{\partial \tau_{curve}} \Delta \tau = \frac{1}{\tau_{curve}} \Delta s - \frac{s_{curve}}{{\tau_{curve}}^2} \Delta \tau, \tag{32}$$

where $\Delta s = s_{\text{curve}} - s_{\text{straight}}$ and $\Delta \tau = \tau_{\text{curve}} - \tau_{\text{straight}}$.

According to Fig. 19, the lengths of the curved and straight-line paths are determined by the following equations:

$$s_{curve} = R(\theta_1 - \theta_2), \tag{33}$$

and

$$s_{straight} = \sqrt{(z_2 - z_1)^2 + (r_2 - r_1)^2} = \sqrt{(z_2 - z_1)^2 + R^2 (\sin\theta_2 - \sin\theta_1)^2}. \tag{34}$$

To determine the travel time of the curved path, let $[z(s), r(s)]$ represent the circular trajectory of the ray in the depth-range plane. According to Fig. 19 and (31), the following relationship holds:

$$\mathrm{d}s = R\mathrm{d}\theta = \frac{c(z)}{|g| \cos\theta(z)} \mathrm{d}\theta. \tag{35}$$

Applying (30) and (35), the travel time for a circular ray path can be determined as follows:

$$\tau_{curve} = \int \frac{\mathrm{d}s}{c(s)} = \frac{1}{|g|} \int_{\theta_1}^{\theta_2} \frac{\mathrm{d}\theta}{\cos\theta} = \frac{1}{|g|} \left\{ \ln \left| \frac{1 + \sin(\theta_2)}{\cos\theta_2} \right| - \ln \left| \frac{1 + \sin(\theta_1)}{\cos\theta_1} \right| \right\}. \tag{36}$$

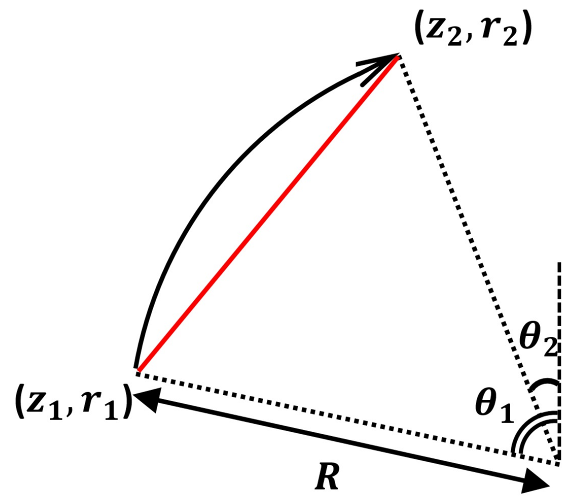

Fig. 19: Arc path and straight-line path with a linear SSP with positive gradient.

As assumed in (1) and (7), which describe straight-line propagation, the travel time for the straight-line ray, $\tau_{straight} = s_{straight}/c_{avg}$, requires calculating the average sound speed using the SSP. Assuming infinitesimally thin layers, the average sound speed for the straight-line ray between depths z_1 and z_2 is given by (26):

$$c_{avg} = \left[\frac{1}{z_2 - z_1}\int_{z_1}^{z_2}\frac{\mathrm{d}z}{c(z)}\right]^{-1}. \tag{37}$$

Considering the linear SSP described in equation (28), we have:

$$c_{avg} = \left[\frac{1}{g(z_2 - z_1)}\ln\frac{c(z_1) + g(z_2 - z_1)}{c(z_1)}\right]^{-1}. \tag{38}$$

Using calculated c_{avg} and ray path determined by (34), the straight-line travel time $\tau_{straight}$ can be obtained.

To illustrate the effect of the straight-line approximation on sound speed estimation for our sampling geometry (Fig. 1), consider an ocean layer with a non-uniform sound speed profile and a thickness of Δz, where the sound speed varies linearly from 1480 m/s to 1520 m/s. Fig. 20 shows the difference in sound speed estimation, Δc_{avg}, that arises from assuming straight-line propagation instead of curved propagation, considering receivers positioned at various ranges for different thicknesses of non-constant sound speed layers.

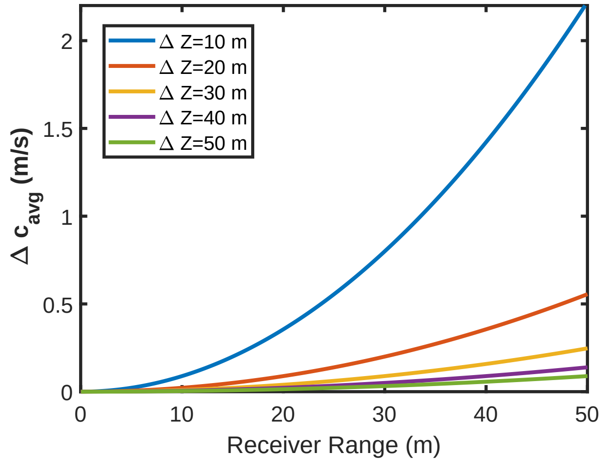

Fig. 20: Difference in sound speed estimation between straight-line and curved propagation assumptions, plotted as a function of receiver range for various layer thicknesses with non-constant sound speed.

As shown in Fig. 20, the assumption of straight-line propagation remains valid even with relatively large sound speed gradients (small Δz in Fig. 20), as long as the angles between the rays and the vertical line to the transducers are kept small. Such small angles can be achieved by limiting receiver ranges to short distances, such as less than 20 m in Fig. 20.

REFERENCES

[1] M. R. Mousavi and L. Zedel, "Ocean sound speed profile measurement using echo arrival times," in *OCEANS 2024 - Halifax*. IEEE, Sep. 2024, pp. 1–5.

[2] R. D. Huston, "Acoustic phase measurements from volume scatter in the ocean," Ph.D. dissertation, Univ. of Victoria, Victoria, Canada, 1987.

[3] B. H. Brumley, "Method and system for remote sound speed measurement," US Patent US8 625 392B2, Jan., 2014, accessed: 2024-07-08. [Online]. Available: https://patents.google.com/patent/US8625392B2/en

[4] C. Stranne, L. Mayer, T. C. Weber, B. R. Ruddick, M. Jakobsson, K. Jerram, E. Weidner, J. Nilsson, and K. Gårdfeldt, "Acoustic mapping of thermohaline staircases in the arctic ocean," *Sci. Rep.*, vol. 7, no. 1, Nov. 2017.

[5] M. Peña, J. Cabrera-Gámez, and A. C. Domínguez-Brito, "Multi-frequency and light-avoiding characteristics of deep acoustic layers in the north atlantic," *Mar. Environ. Res.*, vol. 154, p. 104842, Feb. 2020.

[6] J. Ophir and T. Lin, "A calibration-free method for measurement of sound speed in biological tissue samples," *IEEE Trans. Ultrason. Ferroelectr. Freq. Control*, vol. 35, no. 5, pp. 573–577, Sep. 1988.

[7] D. E. Robinson, J. Ophir, L. S. Wilson, and C. F. Chen, "Pulse-echo ultrasound speed measurements: Progress and prospects," *Ultrasound Med. Biol.*, vol. 17, no. 6, pp. 633–646, Jan. 1991.

[8] M. E. Anderson and G. E. Trahey, "The direct estimation of sound speed using pulse–echo ultrasound," *J. Acoust. Soc. Amer.*, vol. 104, no. 5, pp. 3099–3106, Nov. 1998.

[9] F. R. Pereira, J. C. Machado, and W. C. A. Pereira, "Ultrasonic wave speed measurement using the time-delay profile of rf-backscattered signals: Simulation and experimental results," *J. Acoust. Soc. Amer.*, vol. 111, no. 3, pp. 1445–1453, Mar. 2002.

[10] D. Napolitano, C. H. Chou, G. McLaughlin, T. L. Ji, L. Mo, D. DeBusschere, and R. Steins, "Sound speed correction in ultrasound imaging," *Ultrasonics*, vol. 44, pp. e43–e46, Dec. 2006.

[11] C. Yoon, Y. Lee, J. H. Chang, T. Song, and Y. Yoo, "In vitro estimation of mean sound speed based on minimum average phase variance in medical ultrasound imaging," *Ultrasonics*, vol. 51, no. 7, pp. 795–802, Oct. 2011.

[12] M. Jakovljevic, S. Hsieh, R. Ali, G. C. L. Kung, D. Hyun, and J. J. Dahl, "Local speed of sound estimation in tissue using pulse-echo ultrasound: Model-based approach," *J. Acoust. Soc. Amer.*, vol. 144, no. 1, pp. 254–266, Jul. 2018.

[13] R. Ali, A. V. Telichko, H. Wang, U. K. Sukumar, J. G. Vilches-Moure, R. Paulmurugan, and J. J. Dahl, "Local sound speed estimation for pulse-echo ultrasound in layered media," *IEEE Trans. Ultrason. Ferroelectr. Freq. Control*, vol. 69, no. 2, pp. 500–511, Feb. 2022.

[14] R. Ali and J. J. Dahl, "Distributed phase aberration correction techniques based on local sound speed estimates," in *Proc. 2018 IEEE Int. Ultrason. Symp. (IUS)*, Oct. 2018, pp. 1–4.

[15] W. Munk, P. Worcester, and C. Wunsch, *Ocean Acoustic Tomography*. Cambridge Univ. Press, 1995.

[16] D. E. Robinson, F. Chen, and L. S. Wilson, "Measurement of velocity of propagation from ultrasonic pulse-echo data," *Ultrasound Med. Biol.*, vol. 8, no. 4, pp. 413–420, Jan. 1982.

[17] D. E. Robinson, C. F. Chen, and L. S. Wilson, "Image matching for pulse echo measurement of ultrasonic velocity," *Image Vis. Comput.*, vol. 1, no. 3, pp. 145–151, Aug. 1983.

[18] N. Hayashi, N. Tamaki, M. Senda, K. Yamamoto, Y. Yonekura, K. Torizuka, T. Ogawa, K. Katakura, C. Umemura, and M. Kodama, “A new method of measuring in vivo sound speed in the reflection mode,” *J. Clin. Ultrasound*, vol. 16, no. 2, pp. 87–93, Feb. 1988.

[19] M. Kondo, K. Takamizawa, M. Hirama, K. Okazaki, K. Iinuma, and Y. Takehara, “An evaluation of an in vivo local sound speed estimation technique by the crossed beam method,” *Ultrasound Med. Biol.*, vol. 16, no. 1, pp. 65–72, Jan. 1990.

[20] J. Ophir, T. Moriya, and Y. Yazdi, “A single transducer transaxial compression technique for the estimation of sound speed in biological tissues,” *Ultrasonic Imaging*, vol. 13, no. 3, pp. 269–279, Jul. 1991.

[21] M. R. Mousavi, M. Karimi, and M. Farrokhrooz, “Statistical properties of high frequency acoustic fluctuations induced by rough sea surface,” in *Proc. 2012 Oceans Conf.*, Oct. 2012, pp. 1–5.

[22] M. R. Mousavi and M. Karimi, “Arrival time and angle fluctuations of sea-surface forward scattering,” *J. Acoust. Soc. Amer.*, vol. 150, no. 2, pp. 694–705, Aug. 2021.

[23] L. Zedel, “Modeling pulse-to-pulse coherent doppler sonar,” *J. Atmos. Ocean. Technol.*, vol. 25, no. 10, pp. 1834–1844, Oct. 2008.

[24] H. Medwin and C. S. Clay, *Fundamentals of Acoustical Oceanography*. San Diego, CA, USA: Academic Press, 1997, available at: https://books.google.com/books?id=kymUKicld2cC.

[25] X. Geng and A. Zielinski, “An eigenpath underwater acoustic communication channel model,” in *Proc. OCEANS ’95 MTS/IEEE Conf.*, vol. 2, 1995, pp. 1189–1196.

[26] W. B. Yang and T. C. Yang, “High-frequency channel characterization for m-ary frequency-shift-keying underwater acoustic communications,” *J. Acoust. Soc. Amer.*, vol. 120, no. 5, pp. 2615–2626, Nov. 2006.

[27] M. R. Mousavi, M. Karimi, and A. Jamshidi, “Probability distribution of acoustic scattering from slightly rough sea surface,” *Ocean Eng.*, vol. 112, pp. 134–144, Jan. 2016.

[28] S. Fielding, G. Griffiths, and H. S. J. Roe, “The biological validation of adcp acoustic backscatter through direct comparison with net samples and model predictions based on acoustic-scattering models,” *ICES Journal of Marine Science*, vol. 61, no. 2, pp. 184–200, 2004.

[29] J. Lubbers and R. Graaff, “A simple and accurate formula for the sound velocity in water,” *Ultrasound in Medicine & Biology*, vol. 24, no. 7, pp. 1065–1068, 1998.

[30] D. E. DiMassa, B. A. Magnell, and J. M. Lund, “Effects of temporal and vertical variability of echo amplitude on adcp selection and performance,” *MTS/IEEE Oceans Conference Proceedings*, vol. 2, pp. 922–929, Oct. 2001.

[31] F. B. Jensen, W. A. Kuperman, M. B. Porter, and H. Schmidt, *Computational Ocean Acoustics*. Springer, 2011.